

# Progress in Large-Eddy Simulation of a Rotor Tip-Clearance Flow

DONGHYUN YOU,<sup>1</sup> RAJAT MITTAL,<sup>2</sup> MENG WANG<sup>1</sup>  
AND PARVIZ MOIN<sup>1</sup>

<sup>1</sup>*Center for Turbulence Research, Stanford University, Stanford, CA 94305*

<sup>2</sup>*Department of Mechanical and Aerospace Engineering, The George Washington  
University, Washington, DC 20052*

A large-eddy simulation (LES) solver which combines an immersed-boundary technique with a curvilinear structured grid has been developed to study the temporal and spatial dynamics of a rotor tip-clearance flow, with the objective of determining the underlying mechanisms for low pressure fluctuations downstream of the rotor near the endwall. Salient feature of the numerical methodology, including the mesh topology, the treatment of numerical instability for non-dissipative schemes in a highly skewed mesh, and the parallelization of the code for shared memory platforms are discussed. Qualitative agreements have been observed between present LES and experimental measurements. The simulations indicate that the interaction between the moving endwall boundary layer and blade boundary layers and tip-leakage flow creates a highly complicated flow which is dominated by distinct vortical structures including the tip-leakage and tip-separation vortices. These vortical structures are found to convect downstream, expand in size and generate intense turbulent fluctuations in the endwall region.

---

## 1. Introduction

In liquid handling systems like axial pumps and ducted propellers (Fig. 1), low pressure fluctuations downstream of the rotor in the vicinity of the endwall can induce cavitation which can lead to structural damage and undesirable acoustic noise. To understand the mechanisms for cavitation, it is necessary to study the detailed turbulence dynamics in the rotor blade wake and the clearance region between the rotor tip and the endwall casing.

Previous experimental studies (e.g., Wenger et al. [1]; Kameier and Neise [2]) indicate that the low pressure fluctuations can result from the turbulence associated with the tip-leakage vortex. Detailed measurements by Zierke et al. [3] in a high-Reynolds-number pump facility have shown that the relative size of the rotor tip-clearance significantly influences the evolution of tip vortex and resultant cavitation. Pressure measurements of

Kang and Hirsch [4, 5] showed that the tip-leakage vortex dominates much of the endwall flow region. The vortex was found to form close to the suction side of the blade and then move away from the suction side, expanding its size with downstream distance. They also used oil films and paint traces to visualize tip-leakage flow in detail. The formation and size of the tip-leakage vortex highly depend on the size of the tip gap. An incompressible compressor cascade study by Storer and Cumpsty [6] with different tip-gap sizes showed that for smaller tip gaps (less than 1.0% of the chord), there was no clear indication of a tip-leakage vortex, while for tip gaps greater than 2.0% of the chord, there is a tip-leakage vortex formed on the suction side of the blade.

Recently, Wang [7] employed a moving endwall in a low-speed linear compressor cascade wind tunnel to mimic the effects of the relative motion between the rotor blade tip and the casing. The results showed significant difference in the formation and the evolution of tip-leakage flows in the moving endwall and the stationary endwall experiments.

Although these previous experiments have provided useful information regarding the tip-clearance flow, significant gaps still exist in our knowledge of the dynamics of the tip-clearance flow as well as the resulting, cavitation inducing low pressure fluctuations. This is primarily due to the difficulty in making detailed measurements near a moving endwall as well as simultaneously measuring velocity, vorticity and pressure. Therefore, a detailed analysis of the unsteady flow in the endwall region downstream of a rotor using time-accurate numerical simulations would go a long way towards improving our understanding of this phenomenon.

Time-accurate simulations of these configurations have been difficult due to the geometric complexity as well as deficiencies of turbulence models in treating highly unsteady flows. Recently, with increasing computing power, the large-eddy simulation (LES) technique, in which resolved and subgrid-scale motions are defined by a spatial filter applied to the Navier-Stokes equations, has emerged as a promising tool which complements Reynolds-averaged Navier-Stokes (RANS) computations. LES is especially suited for this type of flow; the Reynolds numbers are relatively low ( $O(10^5)$ ) which brings these flows within the reach of this modeling approach and also, LES provides detailed spatial and temporal information regarding a wide range of turbulence scales which is precisely what is needed to gain better insight into the flow physics of this configuration. The objective of this project is to develop large-eddy simulation capability for flows through an axial flow rotor with tip-clearance, and to gain a physical understanding of the unsteady flow characteristics in the endwall region downstream of the rotor. In order to provide strong validation for the current study, it was decided to simulate flow in a configuration matching the experimental setup of Devenport's group at Virginia Tech. [7].

It should be pointed out that despite the seeming simplicity of the chosen configuration, these are some of the most complex and ambitious large-eddy simulations attempted to date. At the outset, it was estimated that each simulation would require a grid with  $O(10^7)$  points and  $O(10^5)$  time steps which would translate to  $O(10^5)$  single-node CPU hours per simulation. In addition, each simulation would require over 10GB of memory and over a Terabyte of disk space. Therefore, these simulations are only feasible on large-scale parallel computers. In the current paper, we describe in detail the numerical and computational aspects of the LES flow solver developed for the tip-gap

flow and this is followed by a discussion of some preliminary results from ongoing simulations.

## 2. Simulation Methodology

### 2.1 Numerical Method

The numerical method is based upon the generalized-coordinate Navier-Stokes solver originally developed by Choi et al. [8], with significant enhancements to treat the special difficulties associated with the tip-clearance flow. The spatially filtered Navier-Stokes equations for resolved scales in LES are as follows:

$$\frac{\partial \bar{u}_i}{\partial t} + \frac{\partial}{\partial x_j} \bar{u}_i \bar{u}_j = -\frac{\partial \bar{p}}{\partial x_i} + \frac{1}{\text{Re}} \frac{\partial}{\partial x_j} \frac{\partial \bar{u}_i}{\partial x_j} - \frac{\partial \tau_{ij}}{\partial x_j}, \quad (1)$$

$$\frac{\partial \bar{u}_i}{\partial x_i} = 0, \quad (2)$$

where  $\tau_{ij}$  is the subgrid scale (SGS) stress tensor. All the coordinate variables, velocity components, and pressure are nondimensionalized by the total chord  $C$ , the freestream velocity  $U_\infty$ , and  $\rho U_\infty^2$ , respectively. The time is normalized by  $C/U_\infty$ . The governing equations (1) and (2) are rewritten in a conservative form in generalized coordinates. The dependent variables in the transformed Navier-Stokes equations are volume fluxes across the faces of the cells, which are equivalent to using the contravariant velocity components on a staggered grid multiplied by the Jacobian of the coordinate transformation. Using this choice, the discretized mass conservation can be easily satisfied. The terms in the transformed equations are described in detail in Ref. [8]. The key feature of the numerical method is the use of a non-dissipative, central difference spatial discretization scheme which has been demonstrated to be crucial for retaining the accuracy and predictive capability of the LES approach [9, 10].

The SGS stress tensor  $\tau_{ij}$  is modeled by a Smagorinski type eddy-viscosity model. Given that the tip-clearance flow is fully three-dimensional with no homogeneous directions, the Lagrangian dynamic SGS model [11] is employed. The Lagrangian dynamic model averages the model coefficient along the flow pathlines as opposed to the homogeneous flow direction in the standard dynamic model [12].

The integration method used to solve the transformed governing equations is based on a fully-implicit fractional step method which avoids the severe time-step restriction in the tip-clearance region. All terms including cross-derivative diffusion terms are advanced in time using the Crank-Nicolson method in time and are discretized by the second-order central-difference in space. A Newton iterative method is used to solve the discretized nonlinear equations. Since the widely used semi-implicit method which combines the 3rd order Runge-Kutta and Crank-Nicolson schemes need three evaluations of the Poisson equation, which is the most expensive part of the flow solver per effective time step, it

becomes more expensive than the present fully-implicit method which solves the Poisson equation only once.

For the pressure Poisson equation, a highly efficient multigrid procedure, which is appropriate for parallelization, is used. Since the Poisson solver is the most expensive part of computation in this fully three-dimensional flow, it is crucial to improve both the convergence ratio and the parallel efficiency. By experimenting with various solution methods, we found that a combination of the red-black multigrid method in two-directions and a tridiagonal solver in the other direction provides the most efficient solution procedure.

The entire simulation code has been optimized and parallelized using message passing directives (OpenMP) for shared memory platforms like SGI Origin 2000 or 3000 and Compaq GS320. Significant effort has been put into optimizing the parallel performance by utilizing cache-management strategies and minimizing data dependency. Figure 2 shows the scaleup achieved on a  $256 \times 256 \times 256$  grid with up to 64 processors of SGI Origin 2000. The scaleup factor ( $S$ ) is defined by the ratio of the wallclock time ( $T_1$ ) from a unit CPU to the wallclock time ( $T_N$ ) achieved using  $N$ -CPU's ( $S=T_1/T_N$ ). The condition of the computer system such as CPU usage and memory usage appears to affect the scaleup within a reasonable range.

## 2.2 Flow Configuration

The flow configuration is schematically shown in Fig. 3. The present study is focused on the rotor blade stage in a linear cascade matching the experimental setup of Wang [7] as shown in Fig. 4. The rotor blade has a small tip-clearance with the endwall. The computational domain is of size  $L_x \times L_y \times L_z = 1.5C \times 0.929C \times 0.5C$  (see Fig. 3 for coordinate definition and Fig. 5 for an  $x$ - $y$  plane), where  $C$  is the chord length. The rotor is placed near the inflow station so as to leave an adequate region for analysis of flow downstream of the rotor. The simulation is performed in a frame of reference attached to the rotor which eliminates the need to incorporate a moving boundary in our computations. This change in reference frames is accomplished by imposing a velocity equal and opposite to the rotor velocity on the incoming flow as well as the endwall. This is consistent with the experiment of Wang [7], where a moving belt is used as the endwall.

Periodic boundary conditions used along the  $y$ -direction allow us to mimic the flow in the interior of a cascade. The  $y$ -direction domain size  $L_y = 0.929C$  is chosen so as to be consistent with the experiment [7]. Another simplification is made by terminating the blade-span to one-half chord length and imposing inviscid flow boundary conditions on that boundary. This can be justified by observing that the root vortex at the hub does not play any significant role in the convected low pressure fluctuations which are found near the endwalls. In Wang's experiment [7], the tip-leakage vortex extends to about one-quarter of a chord length from the endwall which suggests that a blade-span equal to  $0.5C$  should suffice. The inflow turbulent boundary layer data is provided using the method of Lund et al. [13], modified to account for the fact that the mean flow direction is not perpendicular to the inflow/outflow plane.

No-slip boundary conditions are applied along the rotor blade and moving endwall and the convective boundary condition,

$$\frac{\partial \bar{u}_i}{\partial t} + U_c \frac{\partial \bar{u}_i}{\partial x_1} = 0,$$

is applied at the exit boundary, where the convection speed  $U_c$  is set equal to the mean streamwise velocity integrated across the exit plane.

The blade has a relatively high stagger-angle of about 57 degree (see Fig. 4). This high stagger angle generates very skewed mesh and requires fine control of mesh parameters such as the grid stretching ratio and mesh cell aspect ratio. The size of the tip-clearance is 1.6% of the total chord, blade pitch is 0.9 chord, and the blade span is 0.5 chord. The Reynolds number of this flow is 400,000 based on the chord and freestream velocity, and the inflow turbulent boundary layer has a Reynolds number of 780 based on the momentum thickness.

The full computational domain and grid distribution in a plane perpendicular to the blade (parallel to the endwall) is shown in Fig. 5. The third direction is Cartesian with non-uniform grid distributions. Since the main interest of the study is in the downstream turbulence, the computational domain is extended to 1.5 chord length beyond the trailing edge.

### *2.3 Mesh Topology and Immersed Boundary Method*

The presence of the tip-clearance region between the rotor tip and the endwall presents considerable difficulty in grid topology and resolution and in fact has been a major obstacle to the accurate prediction of this flow. A commonly used mesh topology is the “embedded  $H$ -type mesh” (e.g., Ref. [14]). However, the embedded  $H$ -mesh has significant drawbacks. As shown in Fig. 6, the blade surface in an  $x$ - $y$  plane is mostly represented by longitudinal grid lines except near the leading and trailing edges, where it is represented by the transverse grid lines. The number of longitudinal grid lines below the airfoil and in the tip region is determined by the resolution requirements in the tip-gap. This causes the convergence of the longitudinal grid lines in the leading and trailing edge regions, leading to high aspect and stretching ratios, which are inappropriate for non-dissipative numerical schemes [10, 15]. The extremely small  $y$  grid spacing in these regions imposes severe restrictions on the allowable time-step size.

In recent years the immersed boundary method [16] has emerged as a flexible and efficient tool for treating boundary conditions in complex geometries. With this approach, the simulations can be carried out on a simple grid, and boundary conditions are assigned by applying body forces to the momentum equations to mimic the effect of the boundary. Because of the need to resolve the thin turbulent boundary layers, the immersed boundary method works best if one set of grid lines are parallel or nearly parallel to the boundary, which is not feasible on a Cartesian mesh for the present configuration.

To overcome the above difficulties, a novel approach which combines an immersed boundary technique [16] with a structured grid in generalized curvilinear coordinates is employed to treat the tip-gap region. The advantage of using the immersed boundary method in a curvilinear mesh is that we can generate the grid lines almost parallel to the blade surface. As demonstrated in Fig. 5, the blade surface is nearly parallel to one set of the grid lines, ensuring an adequate resolution of the boundary layers. Periodic boundary conditions are applicable on the curved upper and lower boundaries.

Validation simulations (Fig. 7) of the three-dimensional tip-clearance flow at  $Re_c = 3000$  show satisfactory performance of the method, in terms of resolution and convergence.

#### *2.4 Grid Skewness and Numerical Stability*

The large blade angle coupled with the need to have a periodic grid in the crosstream direction leads to a mesh that is highly skewed over the blade surface. For such mesh topologies, non-dissipative schemes such as the one employed here, tend to exhibit highly enhanced dispersive error which can affect the quality of computed results and sometimes even lead to numerical instability. This was our experience with preliminary simulation in this configuration as well as simulation of flow through a low-pressure turbine [17]. In the past, control of dispersive error and numerical instability is accomplished through the use of upwind scheme or through the explicit addition of numerical viscosity. However, past studies [10] have indicated that such remedies are not appropriate for use in conjunction with LES.

It is well known that numerical instability for non-dissipative schemes is often caused by the high local Peclet numbers, large mesh stretching ratio, large mesh aspect ratio and mesh unsmoothness. However, the effect of mesh skewness has not been well understood. In the current study extensive tests have been carried out in order to examine various aspects related to grid skewness. A test of various formulations of the non-linear convection terms indicated that with a highly skewed mesh, the divergence and skew-symmetric form lead to superior stability characteristics as compared to the rotational form (see Fig. 8).

In addition to this, truncation error analysis indicates that central difference discretization of the Navier-Stokes equations on a highly skewed and stretched mesh leads to spurious negative diffusion terms in the modified equation. Since grid skewness is controlled by the geometry of the blade, the only means of controlling the negative diffusion is through careful control of the grid stretching ratio. In the current simulation, we therefore use meshes where the grid stretching ratio in both direction is kept small. This leads to an increase in the mesh size and consequently the computational resources.

It should be pointed out that grid skewness related problems are usually not observed in conjunction with numerical scheme that employ numerical dissipation (either through upwinding, explicit addition of artificial dissipation or through the use of stabilizers). However, unless carefully controlled, numerical dissipation can also overcome the SGS contribution thereby reducing the accuracy and predictive capability of the LES approach. Furthermore, as shown by Gresho and Lee [18], dissipative schemes do not provide any obvious warning of lack of resolution whereas this is usually quite clear with non-dissipative schemes due to the appearance of the so called “2-Delta” waves. For these reasons, we strongly advocate the use of the non-dissipative schemes for these types of computations despite the increase in computational resources that usually accompanies the use of these schemes.

### 3. Results and Discussion

The newly developed solver is being used to simulate the tip-clearance flow and analyze the three-dimensional flow structures in the tip-clearance and the dynamic interactions of the tip-leakage vortex with the endwall turbulent boundary layer. The mesh sizes used for the simulation are  $321 \times 256 \times 96$  and  $449 \times 350 \times 128$  ( $x \times y \times z$ ). The coarser grid simulation was carried out first and the results of this simulation were examined in detail so as to determine the resolution requirements. The finer mesh was subsequently constructed using this information. Qualitative comparisons have been made between the ongoing LES and the experimental measurements [7] in the downstream location as shown by dashed line in Fig. 4. In the experiments [7], four sets of hot wire measurements were taken to obtain detailed information of the mean and turbulent flow field downstream of the compressor cascade.

Figure 9 represents the overall flow structures from the present LES's and experiments [7] at  $x/C_a = 1.51$  as seen by an observer looking upstream (see Fig. 4). Here  $C_a$  is the axial chord length by which the locations are normalized. Vertical bundles of the mean streamwise velocity contours are present in the wakes of rotor blades, and the tip-leakage vortices are found near the endwall in both the present LES and the experiment [7]. Compared with the experimental findings, the tip-leakage vortex predicted by the LES with  $321 \times 250 \times 96$  mesh (cf. Fig. 9(b)) is smaller in size and its location is shifted in the  $y$ -direction. Examination of the simulation results indicated that this inconsistency was caused in part by the inadequate resolution of the blade suction surface boundary as well as the tip clearance region. Past simulations [19] have shown that inadequate streamwise resolution leads to excess streamwise momentum in turbulent boundary layers making them more resistant to separation. It was felt that increasing the streamwise resolution of the attached blade boundary layer would lead to earlier separation both from the blade surface and the tip region thereby increasing the size and strength of the vortex structures. Based on these observations, a finer mesh of  $449 \times 350 \times 128$  was constructed. The simulation of this finer mesh is not complete at the time this paper was written so we present here only preliminary results

Figure 9(a) shows the corresponding mean streamwise velocity plot for this finer mesh simulation. It is clear that the finer mesh computation indeed predicts a vortex topology which is more in line with experiments. In particular, the size of the vortex structure is quite comparable to that in the experiment although there is still a mismatch in the location of the structure. However, it should be pointed out that the fine mesh plot shown corresponds to an early time in the simulation and the structure is expected to move to the right as the simulation proceeds further thereby moving the simulation results closer to the experiment. It should also be pointed out that currently the sample time for computing the statistics is quite small and that also is expected to contribute the inconsistency between the simulation and experiments.

The energy spectra from the  $321 \times 250 \times 96$  mesh run in the tip-leakage region ( $x=1.51C_a$ ,  $y=1.4C_a$ ,  $z=0.1C_a$ ) are shown in Fig. 10. The spectra from both the LES and the experiment clearly show presence of the inertial subrange. From the spectral peaks, we may expect distinct coherent motions in the tip-leakage flow. The present numerical scheme appears good in resolving low to intermediate frequency energies without

excessive numerical dissipation. However, the predicted spectra drop off too rapidly at higher frequencies, indicating a lack of spatial resolution which affects the high frequency components through Taylor's hypothesis. This lack of grid resolution, which is particularly severe in the streamwise direction, may have caused a premature breakdown of the tip-leakage vortex, contributing to the smaller vortex sizes observed in Fig. 9(b).

Figure 11 shows the instantaneous and time-averaged pressure contours in  $x$ - $y$  plane very close to the moving endwall ( $z=0.008C_d$ ) obtained with the fine mesh. The spatial variations of the negative pressure relative to the mean values appear to be highly correlated with the tip-leakage flow and could potentially trigger cavitation events. These results indicate that a strong circular motion is developed by the tip-leakage vortex around the low-pressure core and this structure travels downstream expanding the size and generating intense fluctuations in the endwall region.

Figure 12 shows instantaneous streamwise velocity contours in  $x$ - $y$  planes (see Fig. 3 for coordinate definition). Very close to the endwall (left figures), negative streamwise velocity contours are dominant due to the tip-leakage vortex driven by the pressure gradient between the pressure side and suction side of the blade. On the other hand, far from the endwall (right figures), the contour plot shows two-dimensional like blade boundary-layer separations. The effects of grid resolution are apparent in these contour plots. In the  $449 \times 350 \times 128$  mesh run (Fig. 12(a)), the intensity of the tip-leakage flow is higher than that of the  $331 \times 250 \times 96$  mesh run (Fig. 12(b)). Also, the refined mesh simulation shows less diffusive evolution of the vortical structures in the downstream direction.

The vortex interaction appears more clearly in the instantaneous negative pressure iso-surfaces as a sequential time series in both the fine and coarse mesh simulations (Fig. 13). The negative pressure iso-surfaces which reveal typical vortex structures in the tip-clearance flow are found from the simulation. The tip-leakage vortex has a nearly circular core with high total pressure loss and low static pressure value, and is observed to evolve close to the endwall and to the suction side of the flow passage. Also observed are smaller vortices such as the tip-separation vortex and secondary vortices around the edges of a blade, which have also been observed in the experiments of Wang [7] and other investigators. The complexity of the vortical structures around the blade surface is further increased by the interaction between the tip-leakage vortex and the nearly two-dimensional separations on the suction side surface, thus creating extremely complex low-pressure fluctuations. A comparison of the structures for the coarse and fine mesh cases clearly shows that as expected, the increased resolution of the attached boundary layer results in upstream movement in the location of the tip-leakage vortex and the blade suction surface separation. This movement changes significantly the flow in the downstream region and moves the simulation results closer to the experiment.

## 4. Conclusions

In order to analyze the temporal and spatial dynamics of the rotor tip-clearance flow and determine the underlying mechanism for the low pressure fluctuations, a large-eddy simulation solver which combines an immersed-boundary technique with a generalized curvilinear structured grid has been developed. Numerical aspects related to the grid skewness have been examined.

Results from a preliminary simulation show that the method is capable of capturing the complex flow features observed in well documented experiments. The flowfield is found to exhibit strong circular motions associated with the tip-leakage and tip-separation vortices. These vortical structures are found to convect downstream, expand in size and generate intense turbulent fluctuations in the endwall region. Strong pressure fluctuations which may be responsible for the cavitation and acoustic noise have also been observed. Some quantitative agreements with experiments in terms of velocity and energy spectra have also been observed in the regions close to the rotor blade. However, the agreement deteriorates at downstream locations.

Analysis of the computed results indicates that the improved grid resolution is needed to more accurately describe the evolution of the vortex structures. A new fine mesh simulation is underway. Preliminary results show significantly improved comparison with experimental measurements. In particular the size and location of the tip-leakage vortex downstream of the rotor are better predicted. Once the simulations have been fully validated, the focus will shift to (a) flow analysis to determine the underlying physical mechanism for low pressure fluctuations (b) inclusion of upstream stator blade to include the important “wake cutting” mechanisms (c) inclusion of rotational effects into the computations.

#### *Acknowledgments*

The authors acknowledge the support of the Office of Naval Research under Grant No. N00014-99-1-0389. Computer time was provided by a DoD Challenge Project Grant (C82) through ARL and ASC Major Shared Resource Centers.

#### **References**

- [1] Wenger, C. W., Devenport, W. J., Wittmer, K. S., and Muthanna, C., 1998, “Two-Point Measurements in the Wake of a Compressor Cascade,” AIAA Paper 98-2556.
- [2] Kameier, F., and Neise, W., 1997, “Experimental Study of Tip Clearance Losses and Noise in Axial Turbomachines and Their Reduction,” ASME J. Turbomach., **119**, pp. 460-471.
- [3] Zierke, W. C., Farrel, K. J., and Straka, W. A., 1995, “Measurement of the Tip Clearance Flow for a High-Reynolds-Number Axial-Flow Rotor,” ASME J. Turbomach., **119**, pp. 1-8.
- [4] Kang, S., and Hirsch, C., 1993, “Experimental Study on the Three-Dimensional Flow within a Compressor Cascade with Tip Clearance: Part I-Velocity and Pressure Fields, and Part II-The Tip Leakage Vortex,” ASME J. Turbomach., **115**, pp. 435-443.
- [5] Kang, S., and Hirsch, C., 1994, “Tip Leakage Flow in Linear Compressor Cascade,” ASME J. Turbomach., **116**, pp. 657-664.
- [6] Storer, J. A., and Cumpsty, N. A., 1990, “Tip Leakage Flows in Axial Compressors,” ASME Paper 90-GT-127.
- [7] Wang, Y., 2000, “Tip Leakage Flow Downstream of a Compressor Cascade with Moving End Wall,” MS Thesis, Department of Aerospace Engineering, Virginia Polytechnic Institute and State University.

- [8] Choi, H., Moin, P., and Kim, J., 1992, "Turbulent Drag Reduction: Studies of Feedback Control and Flow over Riblets," Report TF-55, Department of Mechanical Engineering, Stanford University.
- [9] Beaudan, P., and Moin, P., 1994, "Numerical Experiments on the Flow Past a Circular Cylinder at Sub-Critical Reynolds Number," Report TF-62, Department of Mechanical Engineering, Stanford University.
- [10] Mittal, R., and Moin, P., 1997, "Suitability of Upwind-Biased Schemes for Large-Eddy Simulation of Turbulent Flows," *AIAA J.*, **36**, pp. 1415-1417.
- [11] Meneveau, C., Lund, T. S., and Cabot, W. H., 1996, "A Lagrangian Dynamic Subgrid-Scale Model of Turbulence," *J. Fluid Mech.*, **319**, pp. 233-242.
- [12] Germano, M., Piomelli, U., Moin, P., and Cabot, W. H., 1991, "A Dynamic Subgrid-Scale Eddy-Viscosity Model," *Phys. Fluids A* **3**, pp. 1760-1765.
- [13] Lund, T. S., Wu, X., and Squires, K. D., 1998, "Generation of Turbulent Inflow Data for Spatially-Developing Boundary Layer Simulations," *J. Comp. Phys.*, **140**, pp. 233-258.
- [14] Kunz, R. F., Lakshminarayana, B., and Basson, A. H., 1993, "Investigation of Tip Clearance Phenomena in an Axial Compressor Cascade Using Euler and Navier-Stokes Procedures," *ASME J. Turbomach.*, **115**, pp. 453-467.
- [15] Thompson, J. F., Warsi, Z. U. A., and Mastin, C. W., 1985, *Numerical Grid Generation: Foundation and Applications*, North-Holland.
- [16] Fadlun, E. A., Verzicco, R., Orlandi, P., and Mohd-Yusof, J., 2000, "Combined Immersed-Boundary Finite-Difference methods for Three-Dimensional Complex Flow Simulations," *J. Comp. Phys.*, **161**, pp. 35-60.
- [17] Mittal, R., Venkatasubramanian, S., and Najjar, F. M., 2001, "Large Eddy Simulation of Flow Through a Low-Pressure Turbine," *AIAA Paper* 2001-2560.
- [18] Gresho, P. M., and Lee, R. L., 1981, "Don't Suppress Wiggles – They're Telling You Something," *Computers & Fluids*, **9**, pp. 223-253.
- [19] Kaltenbach, H.-J., Fatica, M., Mittal, R., Lund, T. S., and Moin, P., 1999, "Study of Flow in a Planar Asymmetric Diffuser Using Large-Eddy Simulation," *J. Fluid Mech.*, **390**, pp. 151-185.

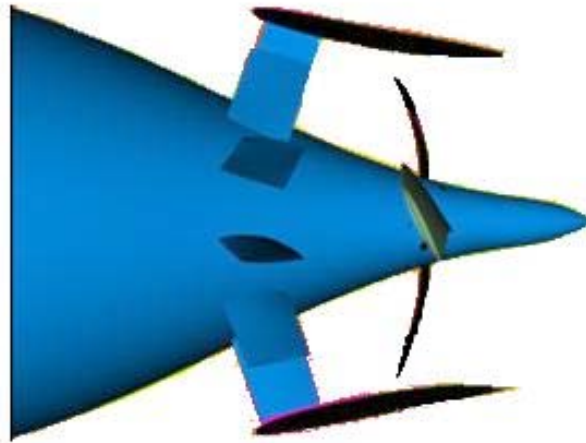


Figure 1: Example of a ducted propeller with tip-clearance.

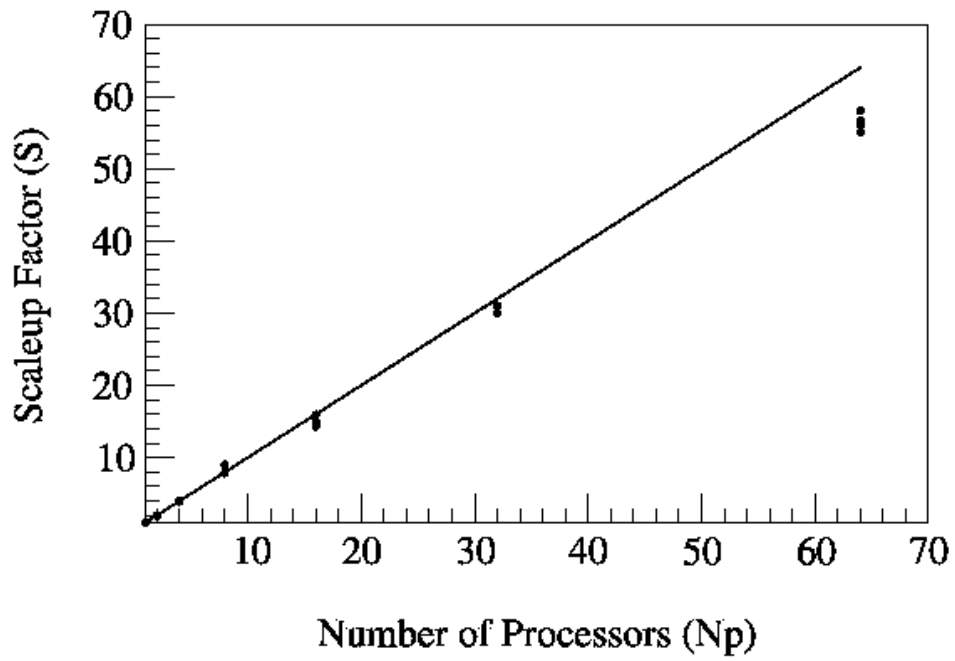


Figure 2: Parallel performance of the solver on a SGI Origin 2000 platform. The solid line represents linear scaleup and symbols represent actual scaleup.

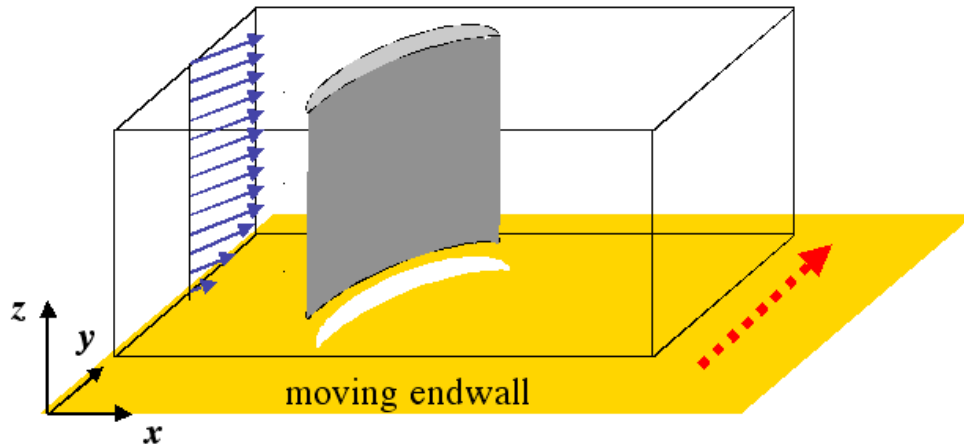


Figure 3: Schematic of flow configuration for LES of a rotor tip-clearance flow.

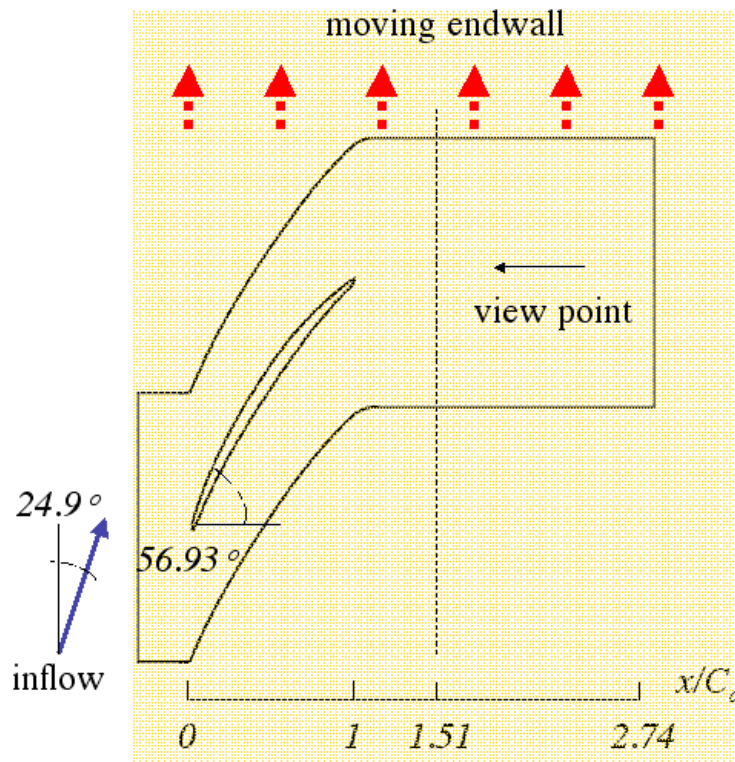


Figure 4: Plane view of the flow configuration. The setup is identical to the linear cascade in the experiment of Wang [7]. The dashed line is the measurement plane where comparisons are made between LES and experiment.  $C$  is total chord length and  $C_a$  is axial chord length.

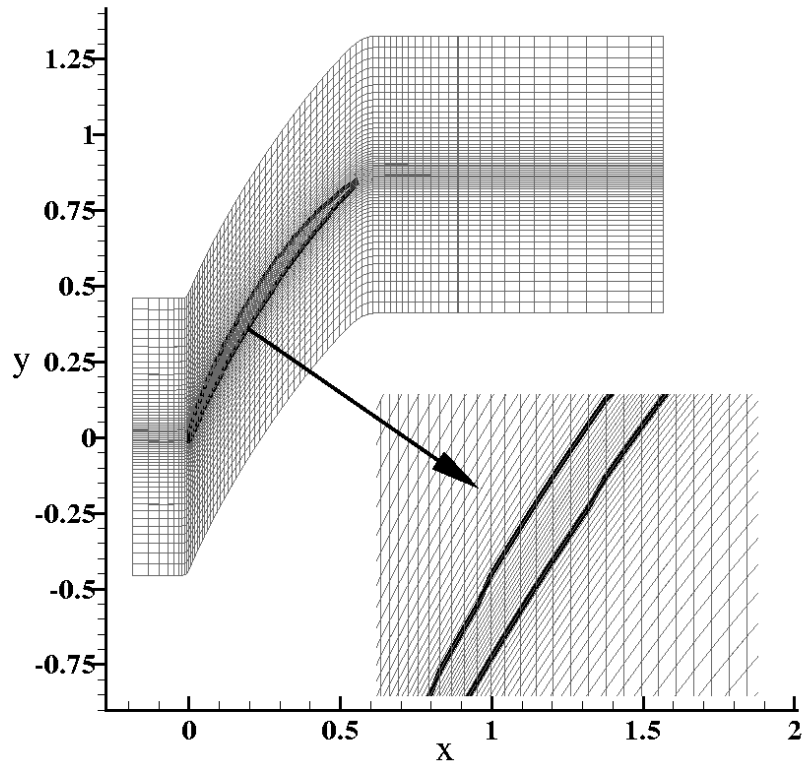


Figure 5: Full computational domain and curvilinear mesh in the  $x$ - $y$  plane used in conjunction with immersed boundary method for tip-clearance flow (1/6 lines are plotted).

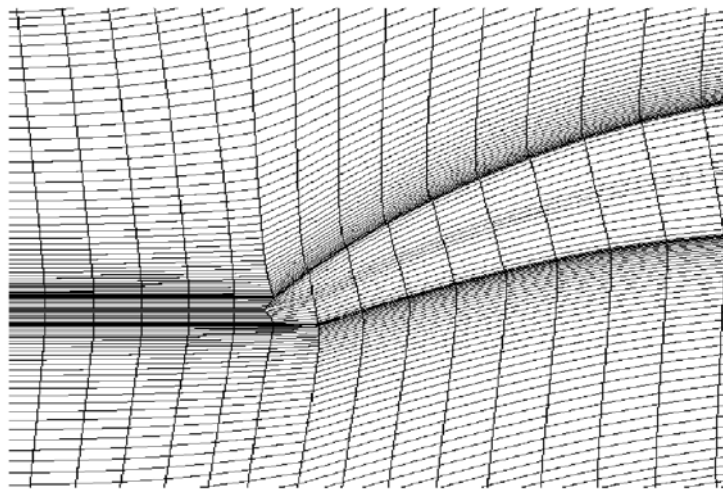


Figure 6: Example of an embedded  $H$ -mesh near the blade leading edge.

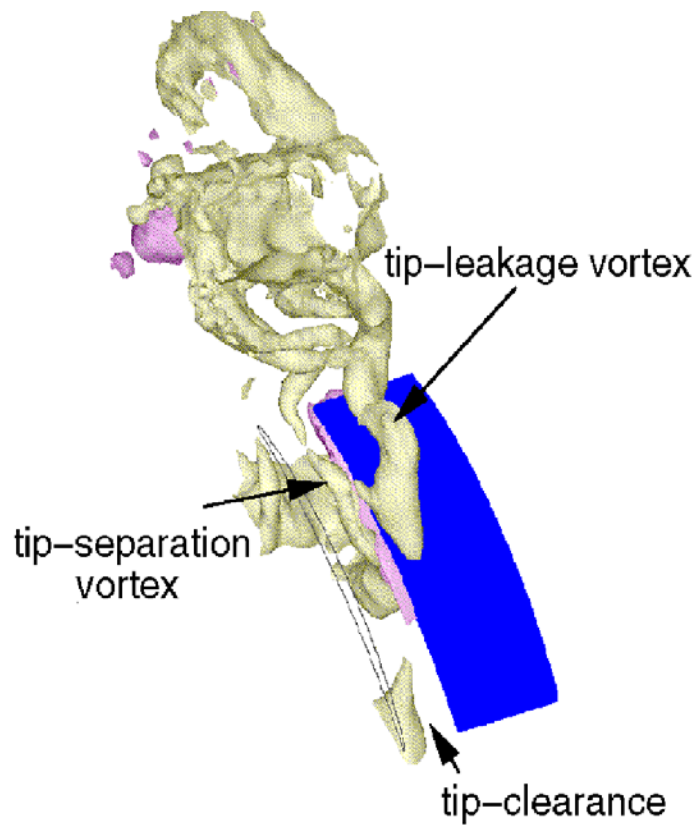


Figure 7: Iso-pressure surfaces from a simulation at  $Re_c = 3000$ .

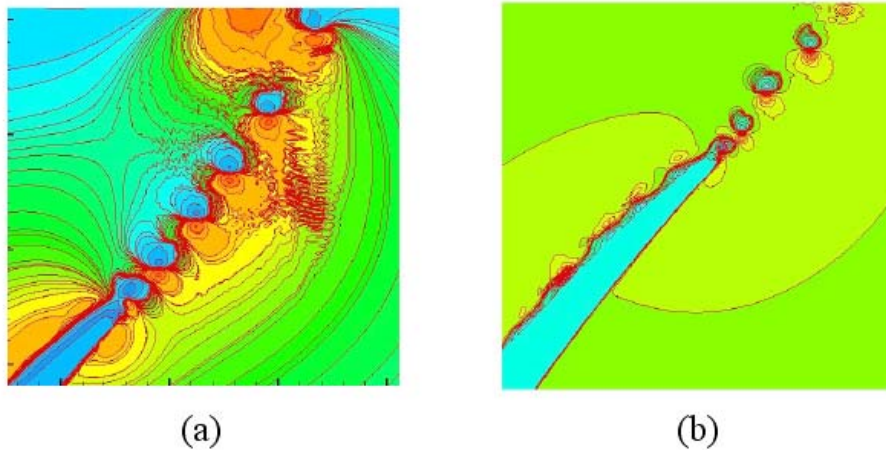


Figure 8: Streamwise velocity contours from two-dimensional simulations using different formulations of convective terms. (a) rotational form; (b) divergence form.

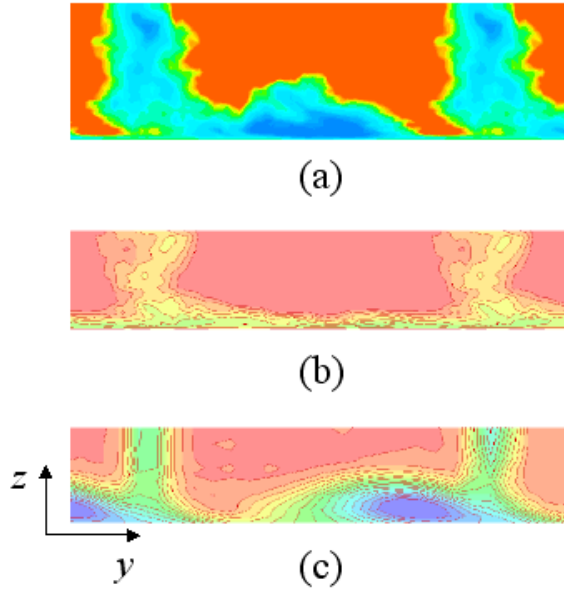


Figure 9: Contour plots of mean streamwise velocity at  $x/C_a = 1.51$ . (a)  $448 \times 350 \times 128$  mesh; (b)  $321 \times 250 \times 96$  mesh; (c) experiment. Contour levels are from 0.45 to 0.8 by 0.0175.

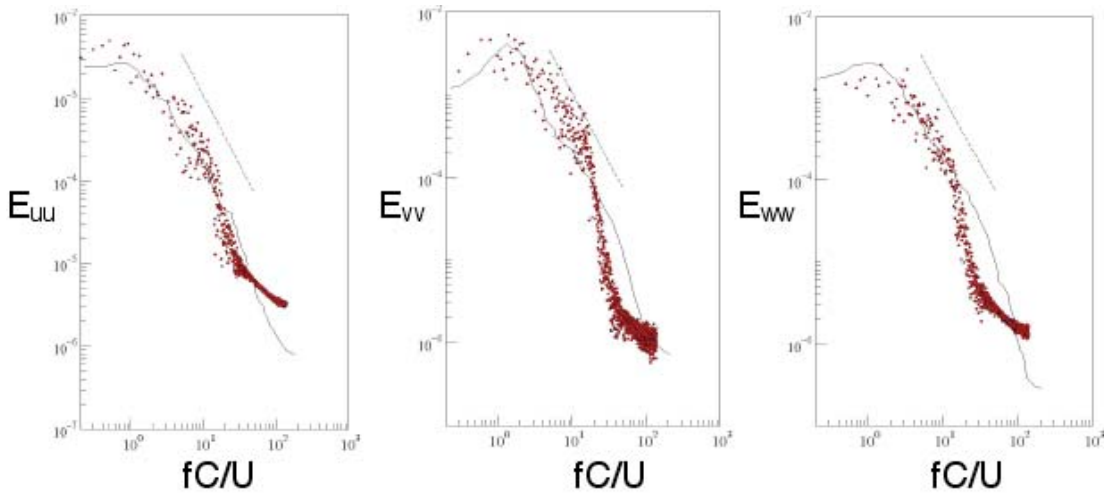


Figure 10: Energy spectra as a function of frequency in the tip-leakage region at  $x/C_a = 1.51$ ,  $y/C_a = 1.4$ ,  $z/C_a = 0.1$ . (a)  $E_{uu}$ ; (b)  $E_{vv}$ ; (c)  $E_{ww}$ . Symbols are from LES with  $321 \times 250 \times 96$  mesh, solid lines are from the experiment [7], and dashed lines are of  $-5/3$  slope.

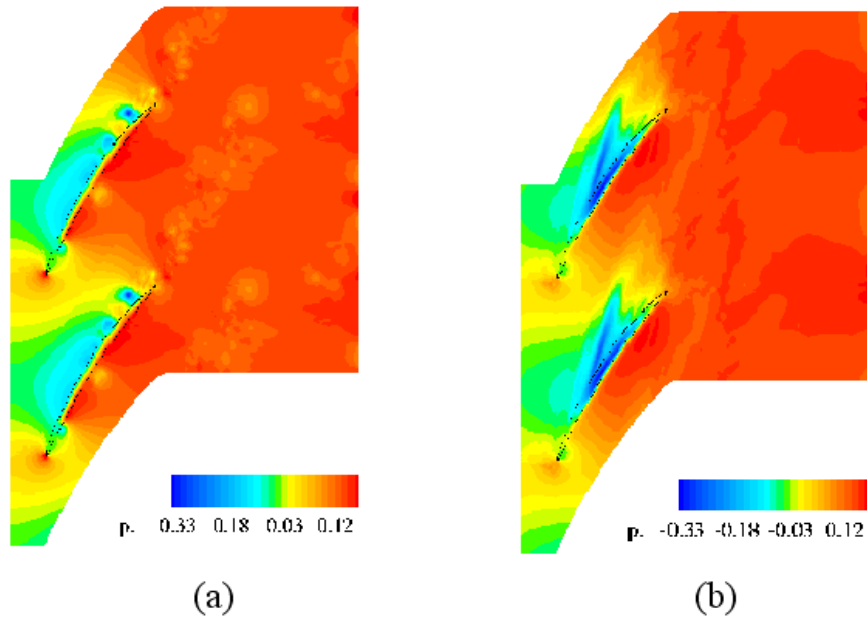


Figure 11: (a) Instantaneous and (b) time-averaged pressure contours in the tip-gap region ( $z/C_a = 0.008$ ), obtained from the  $449 \times 350 \times 128$  mesh simulation.

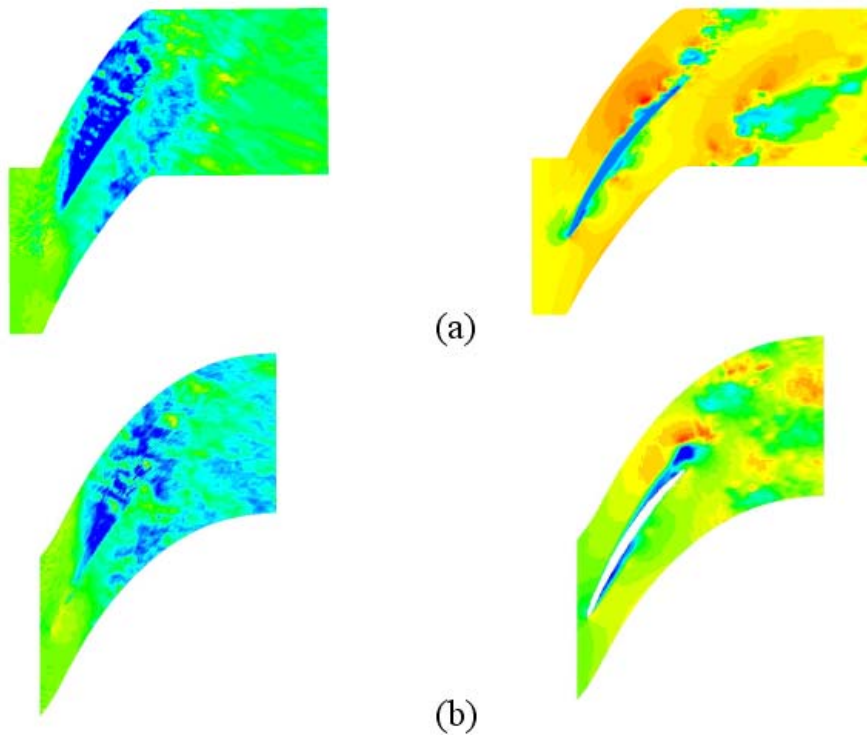


Figure 12: Instantaneous streamwise velocity contours in  $x$ - $y$  planes at  $z/C_a = 0.015$  (left) and  $z/C_a = 0.549$  (right) from (a)  $449 \times 350 \times 128$  mesh and (b)  $321 \times 250 \times 96$  mesh simulations, respectively.

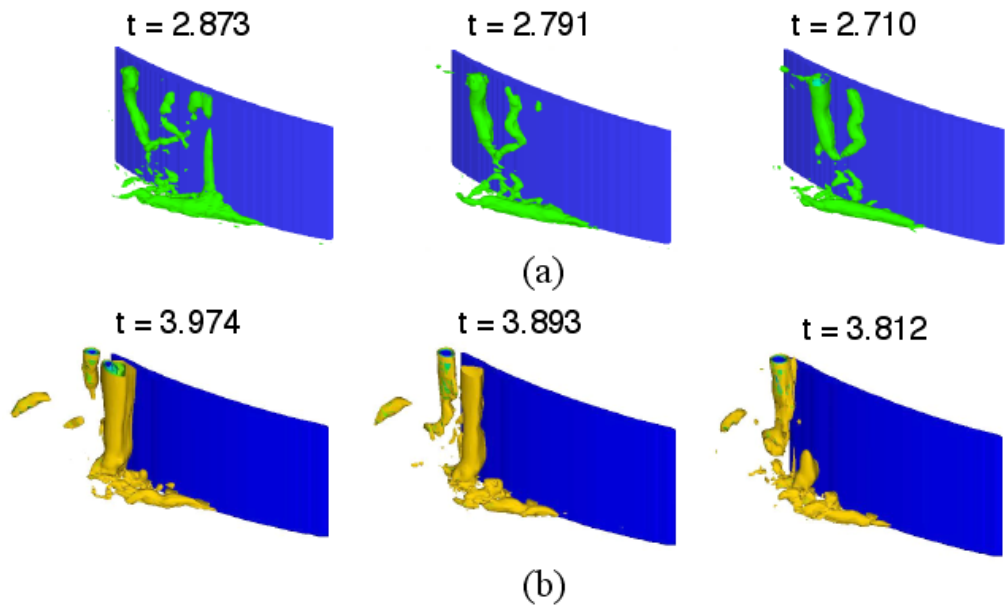


Figure 13: Instantaneous negative pressure iso-surfaces in time series. (a)  $449 \times 350 \times 128$  mesh; (b)  $321 \times 250 \times 96$  mesh simulations. Levels are from  $-0.4$  to  $-0.2$  with increment of  $0.2$ .